Electrochimica Acta 292 (2018) 339–346

Contents lists available at ScienceDirect

Electrochimica Acta

journal homepage: www.elsevier.com/locate/electacta

Carbon-encapsulated $MoSe_2$/C nanorods derived from organic-inorganic hybrid enabling superior lithium/sodium storage performances

Qiong Su [a], Xinxin Cao [a], Xiangzhong Kong [a], Yaping Wang [a], Cheng Peng [b, **], Jing Chen [a], Bo Yin [a], Junrong Shi [a], Shuquan Liang [a], Anqiang Pan [a, *]

[a] School of Materials Science and Engineering, Central South University, Changsha 410083, Hunan, China
[b] Department of Plastic Surgery, The 3rd Xiangya Hospital of Central South University, Changsha 410083, Hunan, China

ARTICLE INFO

Article history:
Received 19 August 2018
Received in revised form
18 September 2018
Accepted 23 September 2018
Available online 25 September 2018

Keywords:
$MoSe_2$/C nanorods
Carbon coating
Bicontinuous electron/ion pathways
Lithium-ion batteries
Sodium-ion batteries

ABSTRACT

Transition metal dichalcogenides (TMDs) have attracted increasing attention for rechargeable batteries because of its high theoretical capacity. However, its real application is limited by the intrinsic low electron conductivity and inferior structural stability. Herein, we report the fabrication of one-dimensional (1D) $MoSe_2$/C nanorods composite from organic-inorganic hybrid $Mo_3O_{10}(C_2H_{10}N_2)$ (named as MoO_x-EDA) with subsequent selenization and carbon coating process. As anode materials for lithium-ion batteries (LIBs) and sodium-ion batteries (SIBs), the carbon-encapsulated composite exhibited enhanced Li^+/Na^+ storage properties compared to $MoSe_2$ nanorods, including good cycling stability and high rate capability. A specific capacity of 835 mA h g^{-1} can be obtained at a current density of 200 mA g^{-1} for the $MoSe_2$/C electrode in LIBs, which retained 755 mA h g^{-1} after 200 cycles. Moreover, a reversible Na^+ storage capacity of 404 mA h g^{-1} can be remained after 100 cycles at a current density of 200 mA g^{-1}. The good electrochemical performances of the $MoSe_2$/C nanorod composites can be attributed to the bicontinuous electron/ion pathways, low charge transfer resistance, and robust structure stability.

1. Introduction

Rechargeable batteries have widely explored as clean environmental benign electrochemical energy storage devices and attracted great attention to meet the challenges of the fossil energy crisis and environmental pollution problems [1,2]. LIBs have dominated the power market for high-tech electronic devices and become the main power system for electrical vehicles because of their high energy density and power capability [3–5]. However, graphite as the state-of-the-art anode material for LIBs has a low theoretical specific capacity (372 mA h g^{-1}) [6–8]. Recently, SIBs as an alternative power system are also extensively studied due to their abundant sodium resources. However, the larger ionic radius of Na^+ (1.06 Å) compared with Li^+ (0.76 Å) will result in the sluggish Na^+ diffusion and large volume variations during the de/intercalation process [9–12]. Many anode materials from LIBs can not work well for SIBs. Therefore, it is urgent to explore alternative anode materials with larger capacity to meet the demands for consumer electronics and the electrification of transportation [3,13–15].

More recently, TMDs with lamellar structures have attracted increasing attention because of their high theoretical capacity and good rate capability [7,16–18]. As a typical TMDs type, $MoSe_2$ has a sandwich-like structure, and the individual layers are held together by weak van der Waals forces [19,20]. The interlayer spacing of $MoSe_2$ is 0.65 nm, remarkably larger than that of graphite (0.34 nm), and can ensure efficient Li^+/Na^+ insertion/extraction, which may be an important characteristic in demonstrating excellent electrochemical behaviors in LIBs/SIBs [21]. Besides, $MoSe_2$ possesses a high theoretical capacity of 422 mA h g^{-1}, which is another advantage for battery configuration [22,23]. However, the electrochemical performances of $MoSe_2$ are limited by the large volume expansion and low electronic conductivity [24]. Great efforts have been endeavored to make $MoSe_2$ and conductive

* Corresponding author.
** Corresponding author.
E-mail addresses: pcheng83@csu.edu.cn (C. Peng), pananqiang@csu.edu.cn (A. Pan).

https://doi.org/10.1016/j.electacta.2018.09.154
0013-4686/

material composites to improve the electrochemical properties [25]. Liu et al. reported sheet-like $MoSe_2$/C composites with a reversible capacity of 576.7 mA h g^{-1} at 100 mA g^{-1} after 50 cycles in LIBs [26]. $MoSe_2$ was grown on carbon fibers to form nanocomposites, which delivered reversible capacities of 610.8 and 347.1 mA h g^{-1} as anode material for LIBs and SIBs after 100 cycles at a current density of 100 mA g^{-1}, respectively [21]. The results demonstrate the electrochemical performances can be greatly improved by making the nanocomposites. However, the packing density of these electrodes may be quite low because of their high surface area and large carbon weight percentages.

Herein, we report a facile synthesis of $MoSe_2$/C nanorods with low surface area. As shown in Fig. 1a, it is different from most of other $MoSe_2$ nanosheets which are obtained by hydrothermal and solvothermal methods with the reaction of Na_2MoO_4, hydrazine hydrate and Se [21–24,26–29], the $MoSe_2$/C nanorods were fabricated via a successive selenization with Se powders (Step II) and *in situ* carbonization with oleic acid as carbon sources (Step III) by using organic-inorganic hybrid MoO_x-EDA nanorods as sacrificial template, which was obtained by a co-precipitation method (Step I) in oil bath. During the selenization process (Step II), the as-prepared nanorod precursor was annealed to crystallize the $MoSe_2$ with the release of organic compounds, along with the generation of a large number of pores. In the process of carbon coating (Step III), the oleic acid on the surface infiltrated into the pores and underwent a process of *in situ* carbonization to form a robust conductive carbon skeleton [30]. As illustrated in Fig. 1b, the conductive carbon scaffolds can provide rapid ion/electron transport and excellent structure stability, resulting in splendid lithium and sodium storage performance.

2. Experimental section

2.1. Materials synthesis

2.1.1. Synthesis of organic-inorganic hybrid material of MoO_x-EDA nanorods

All chemicals and reagents were used as received without further purification. The organic-inorganic hybrid material MoO_x-EDA nanorod were similarly prepared according to previous reports [31–34]. In a typical synthesis, ammonium heptamolybdate ($(NH_4)_6Mo_7O_{24}\cdot 4H_2O$) (1.24 g, 1 mmol) and ethylenediamine (EDA) (0.93 mL, 14 mmol) were dissolved in deionized water (20 mL) in a round-bottom flask. Afterwards, 1 M HCl aqueous solution was slowly dripped to the mixture with magnetic stirring at room temperature until a white precipitate formed (PH 4–5). The temperature was raised to 50 °C in an oil bath for 4 h. The obtained product was filtered and washed several times with deionized water and then dried at 50 °C for 24 h.

2.1.2. Synthesis of $MoSe_2$ nanorods

The as-obtained organic-inorganic hybrid material of MoO_x-EDA nanorod (200 mg, 0.39 mmol) and Se powder (280 mg, 3.55 mmol) were placed in a quartz boat in a tube furnace. After that, the temperature was raised to 600 °C and kept at this temperature for 2 h to finish the reaction under H_2/Ar flow (5% of H_2). The heating ramping rate was set of 3 °C min^{-1}.

2.1.3. Synthesis of $MoSe_2$/C nanorods composite

The above mentioned $MoSe_2$ nanorods (200 mg, 0.79 mmol) and oleic acid (444 mg, 1.57 mmol) were mixed in a 3 mL corundum crucible and stirred at room temperature until the formation of homogenous mixture. Then, the mixture was transferred into a tube furnace and calcinated at 500 °C for 2 h under the flow of Ar atmosphere to get $MoSe_2$/C composite. The temperature ramping rate was set of 3 °C min^{-1}.

2.2. Material characterization

The phases and crystallinity of the samples were recorded by X-ray diffraction (XRD) measurements on a Rigaku D/max 2500 X-ray diffractometer (Cu-Kα, λ = 1.54178 Å). The properties of the carbon coating were analyzed by Raman spectrometer (LabRAM HR800). The weight percentages of carbon in the composite were measured by thermogravimetric (TG) (Netzsch, STA 449C), which were performed in air from 25 to 700 °C at a temperature ramping rate of 10 °C min^{-1}. A field-emission scanning electron microscope (FESEM, FEI Nova NanoSEM 230) and a high-resolution transmission electron microscope (HRTEM, FEI Tecnai F20) were used to characterize the morphologies and microstructures of the samples. X-ray photoelectron spectroscopy (XPS) spectrum of the composite was recorded on the ESCALAB 250Xi.

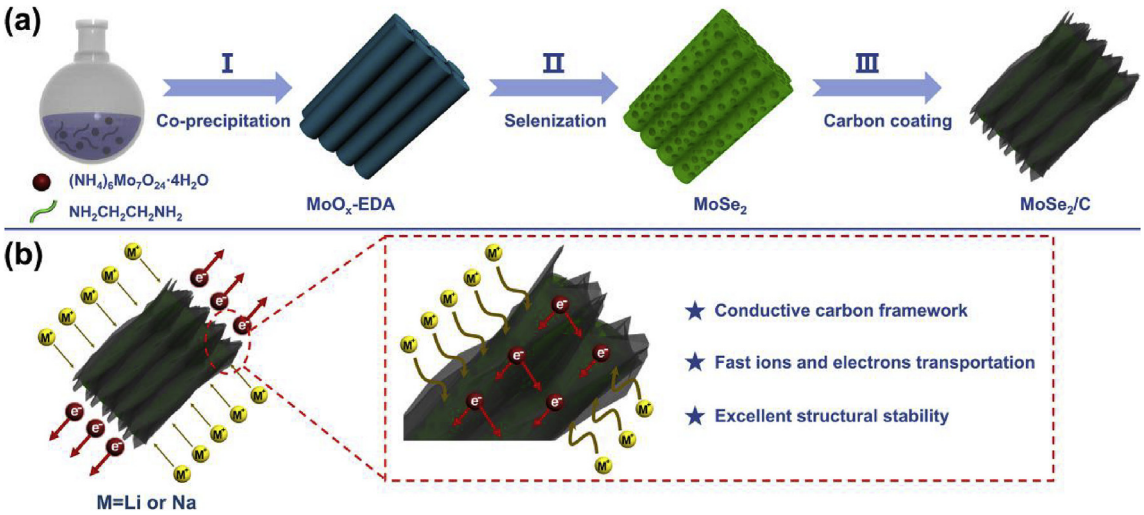

Fig. 1. Schematic illustrations for the fabrication process of $MoSe_2$/C composite as well as the $MoSe_2$/C nanorods with stable framework, fast ion diffusion and high electronic conductivity.

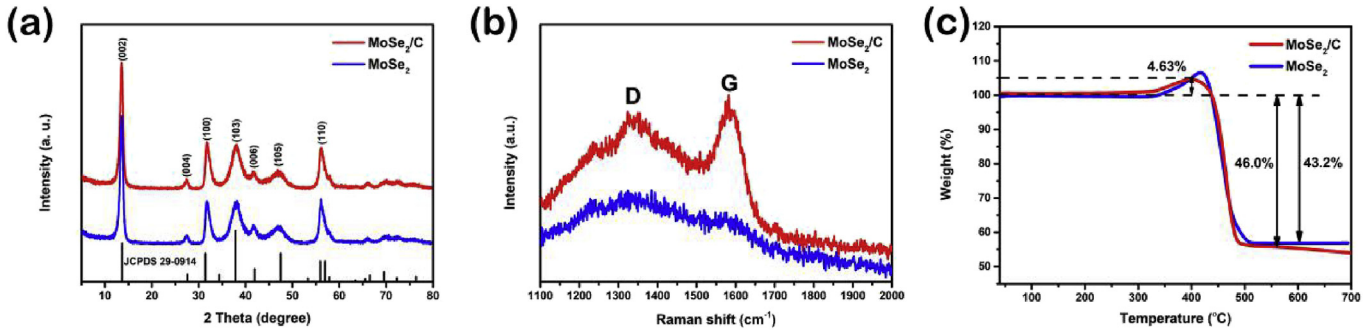

Fig. 2. (a) XRD patterns; (b) Raman scattering spectrum; (c) TG analysis of $MoSe_2$/C and $MoSe_2$ nanorods from room temperature to 700 °C at a heating rate of 10 °C min^{-1}.

2.3. Electrode fabrication and electrochemical measurements

The anode materials, super P and Carboxy Methyl Cellulose (CMC) in a mass ration of 7: 2: 1 were grinded and dispersed in deionized water to get a slurry, which were later spread on Cu foil and dried in vacuum at 80 °C for 12 h. The diameter of the electrode is 12 mm and the loading density of the active material is around 0.8 mg cm^{-2}. All batteries were assembled in a glove box (Shanghai MIKROUNA) filled with ultra-high pure argon. For LIBs assembly, polypropylene membranes and 1 M $LiPF_6$ in ethylene carbonate (EC) – dimethyl carbonate (DMC) – diethyl carbonate (DEC) (1: 1: 1 in volume) were used as a separator and electrolyte, respectively. For SIBs, glass microfiber filters (Whatman GF/D) and 1 M $NaClO_4$ in propylene carbonate (PC) and fluoroethylene carbonate (FEC) mixture solution (95: 5 in volume) were employed as separator and electrolyte, respectively. Cyclic voltammetry (CV) was conducted on a CHI660E (Shanghai Chenhua Instrument Co., China) electrochemical workstation between 0.01 and 3.0 V at a scanning rate of 0.1 mV s^{-1}. All the electrochemical measurements of the as-assembled batteries were tested on a Land Battery Tester (Land CT2001A). The electrochemical impedance spectroscopy (EIS) were recorded on a ZAHNER-IM6ex electrochemical workstation (ZAHNER Co., Germany) in the frequency range of 10^5 Hz–0.01 Hz.

3. Results and discussion

3.1. Structure and morphology characterization

The structures of the obtained materials were characterized and the results are shown in Fig. 2. Fig. 2a presents the XRD patterns of

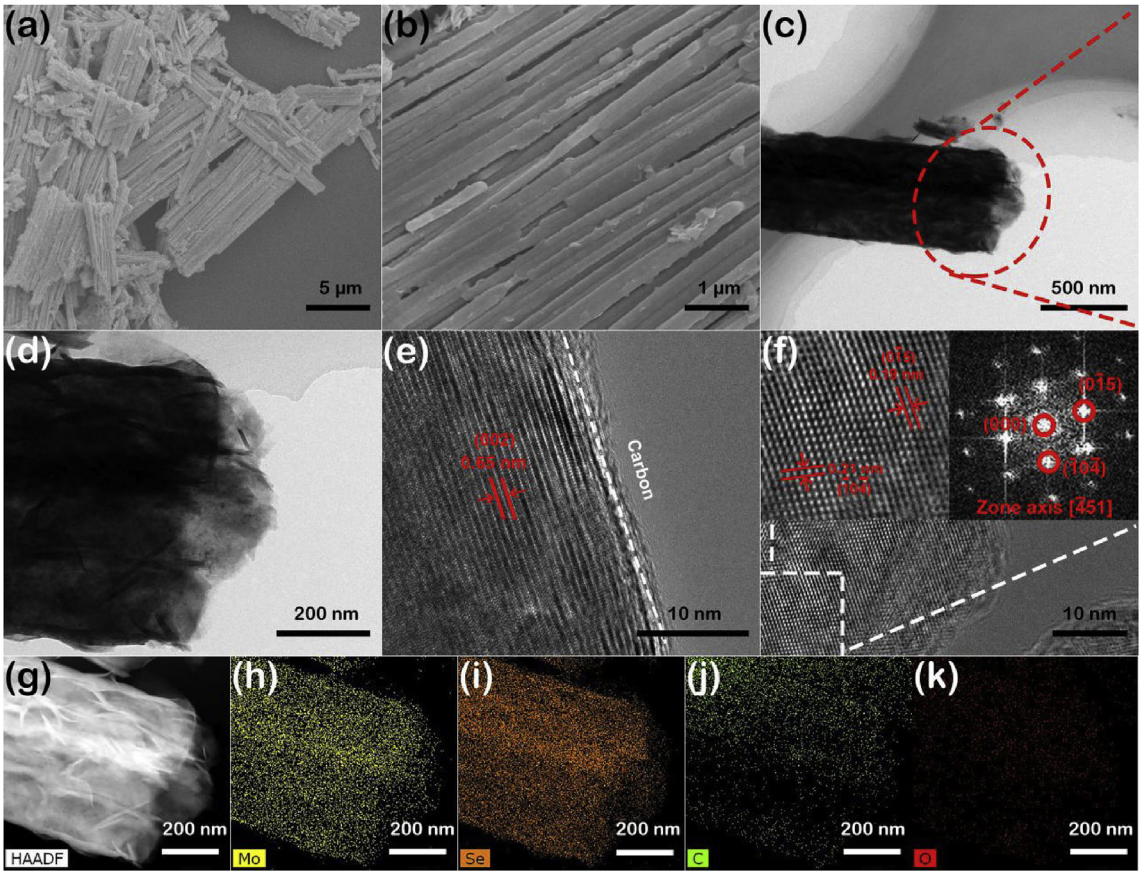

Fig. 3. (a, b) SEM images of $MoSe_2$/C; (c, d) TEM images; (e, f) HRTEM images, the left and the right insets of panel (f) are the magnified pattern and SAED pattern of the selected regions, respectively; (g–k) HAADF-STEM images (C, O, Mo and Se) of $MoSe_2$/C.

$MoSe_2$/C composite and the $MoSe_2$ nanorods. Apparently, all the peaks of $MoSe_2$/C composite and $MoSe_2$ nanorods are matched well with the hexagonal structure of crystalline $MoSe_2$ (JCPDS No. 29–0914). The result indicates organic-inorganic MoO_x-EDA (Fig. S1) has been fully converted into $MoSe_2$ after reaction with Se. According to the primary (002) diffraction peak located at 13.7°, the layer space of $MoSe_2$ is calculated to be 0.65 nm [26,35]. The peak intensity and broadness of the composite are quite similar for both $MoSe_2$ and $MoSe_2$/C composite, indicating the crystallinity and the crystal size do not change much during the followed carbon coating process. Raman spectroscopy of the obtained $MoSe_2$/C composite was shown in Fig. 2b. The peaks at 1339 cm^{-1} and 1582 cm^{-1} can be designated to D-band (the disorder-induce phonon mode) and the G-band (graphite band) for $MoSe_2$/C composite, respectively. D-band and G-band can also be observed but much weaker for $MoSe_2$ at 1337 cm^{-1} and 1588 cm^{-1}, respectively. The $MoSe_2$ nanorods was obtained by annealing the organic-inorganic hybrid material of MoO_x-EDA nanorod and Se powder in H_2/Ar flow, whereas trace carbonization of the organic part happened at the same time. In this work, the I_D/I_G value of $MoSe_2$/C composite is 0.94, which is smaller than that of $MoSe_2$ (1.08), indicating higher graphitization degree for the $MoSe_2$/C composite [10,11,30]. The higher degree of graphitization is beneficial to the better electronic conductivity [36,37]. The content of $MoSe_2$ in $MoSe_2$/C composite was calculated by the TG analysis in Fig. 2c. According to the TG curve for $MoSe_2$/C composite, the weight increases by 4.63% in the temperature range from 300 to 400 °C was attributed to the oxidation of $MoSe_2$ into solid MoO_3 and SeO_2 in the air [21,22]. Subsequently, carbon was oxidized into carbon dioxide accompanied with sublimation of SeO_2 at about 550 °C, resulting in the followed weight loss. Finally, the TG curve tends to be stable when the mass fraction is about 54.0%, and the remainder is MoO_3. In the case of $MoSe_2$ nanorods, 43.2% of weight is lost. Based on these considerations, the weight percentage of carbon in the $MoSe_2$/C composite is estimated to be 4.8%.

As shown in Fig. 3 and Fig. S3, the morphologies and microstructures of $MoSe_2$/C composite and $MoSe_2$ nanorods were investigated by SEM and TEM. The 1D nanorod morphology of organic-inorganic hybrid MoO_x-EDA (Fig. S2) can be retained after selenization (Figs. S3a–S3b). A bundle of $MoSe_2$ nanorods were pictured in Fig. S3c and Fig. S3d, and many pores were observed for nanocrystals (Fig. S3d), which were probably produced by the release of organic compounds during selenization process. The HRTEM images (Fig. S3e and Fig. S3f) clearly shows the distances between two adjacent layers (0.65 nm) for the (002) plane and the interplanar distance (0.24 nm) for the (103) plane of $MoSe_2$, respectively. The different magnification SEM images (Fig. 3a and b) of $MoSe_2$/C composite disclose that the nanorods are arrayed in parallel with a diameter ranging from 200 nm to 600 nm. A TEM image in Fig. 3c shows one individual nanorod decorated with carbon with a diameter about 600 nm, which is well consistent with the SEM images. The nanorod marked in Fig. 3c is magnified and displayed in Fig. 3d. The texture of the nanorod can be seen more explicitly and it seemed that the nanorod is composed of flakes. Oleic acid ($CH_3(CH_2)_7CH=CH(CH_2)_7COOH$), a monounsaturated fatty acid with a high-polarity carboxyl group and a

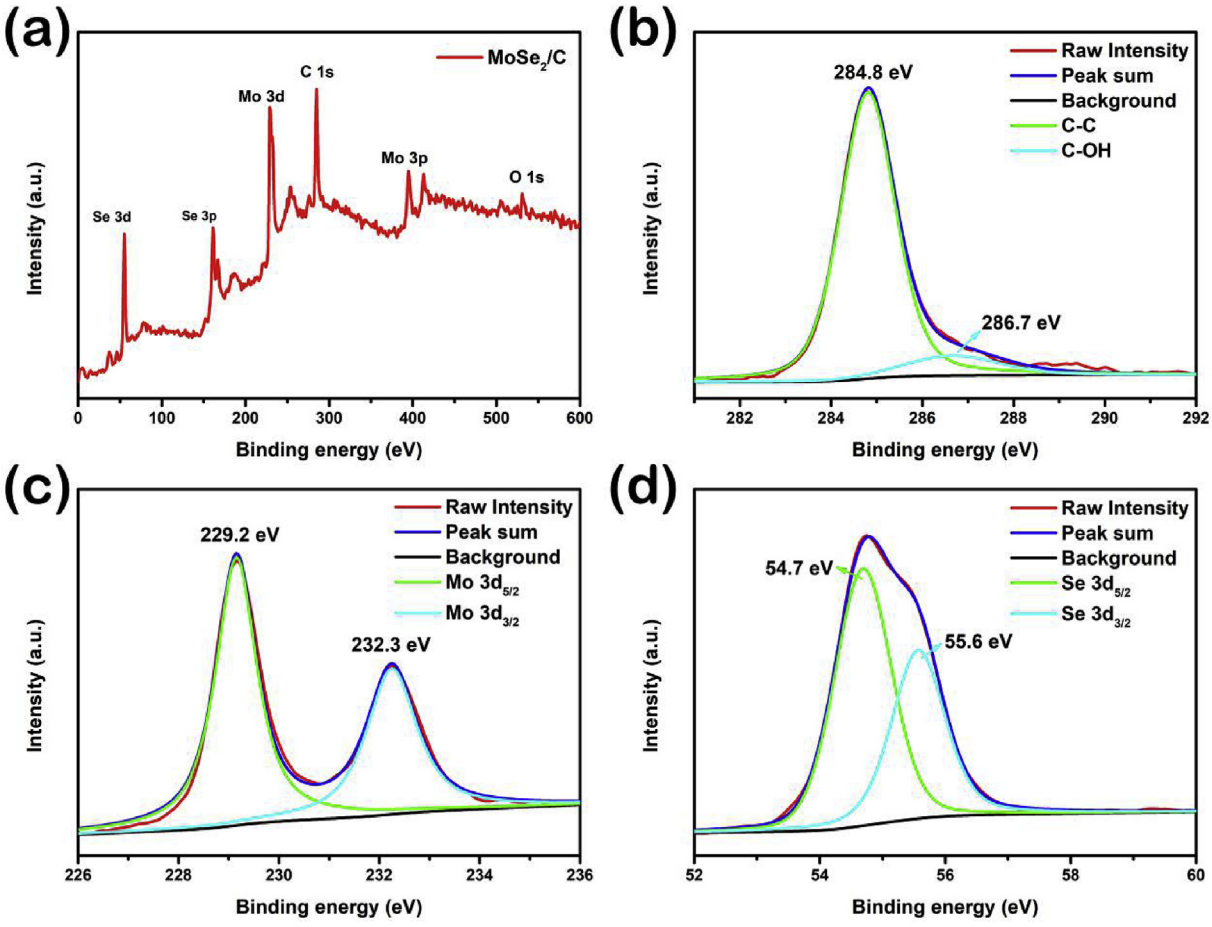

Fig. 4. (a) Survey spectrum; (b) C 1s; (c) Mo 3d; and (d) Se 3d high-resolution XPS spectra of $MoSe_2$/C.

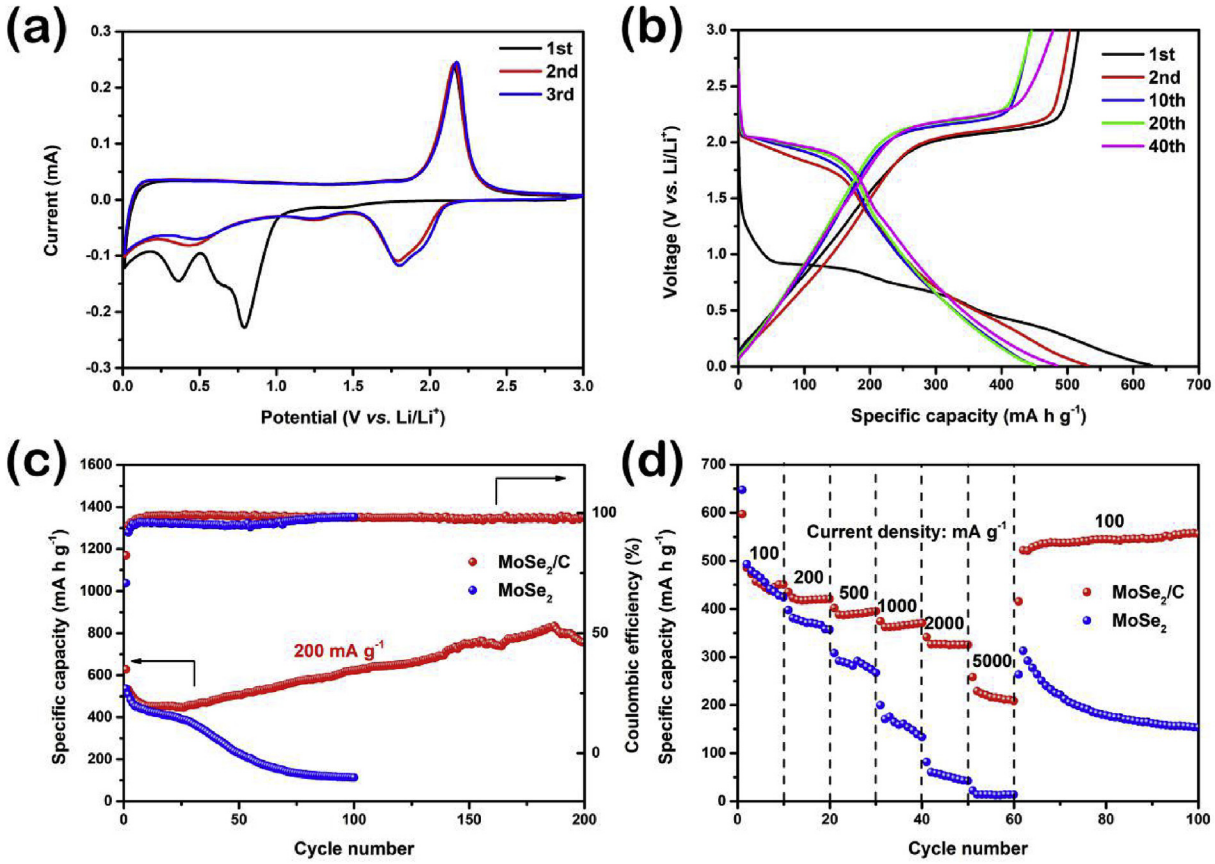

Fig. 5. Electrochemical performances for LIBs: (a) The initial three consecutive CV curves of $MoSe_2$/C at a scanning rate of 0.1 mV s^{-1} between 0.01 and 3 V vs Li/Li^+; (b) GCD profiles of the 1st, 2nd, 10th, 20th and 40th cycle at 200 mA g^{-1}; (c) cycling performances at 200 mA g^{-1}; (d) rate performances at the current densities of 100, 200, 500, 1000, 2000, 5000 mA g^{-1}.

long alkyl chain, plays an important role as a surfactant that can assemble nanocrystals to nanoflakes [10,38]. Fig. 3e–f displays the HRTEM images of the $MoSe_2$/C composite. From Fig. 3e, the interlayer distance is 0.65 nm, which coincides with the (002) plane of the 2H-$MoSe_2$ phase (JCPDS No. 29–0914). A coated carbon layer can also be observed on the surface of the $MoSe_2$. Fig. 3f clearly exhibits the lattice fringes with *d*-spacings of 0.19 and 0.21 nm (the left inset of Fig. 3f), which are consistent with the interplanar distance of the (01(—)5) and (1(—)04(—)) planes of hexagonal $MoSe_2$ crystal, respectively. The selected area electron diffraction (SAED) pattern (the right inset of Fig. 3f) further reveals the single-crystalline nature of $MoSe_2$ and can be indexed to the [4(—)51] zone axis. High angle annular dark field scanning transmission electron microscopy (HAADF-STEM) images in Fig. 3g–k exhibit the homogenous distribution of elements Mo, Se, C and O in nanorod, confirming that $MoSe_2$ is uniformly coated by carbon. It should be noted that element O are originated from the oxygen-containing functional groups on the surface-coated carbon.

Fig. 4 shows XPS result of the as-prepared $MoSe_2$/C composite. The survey spectrum in Fig. 4a presents the coexistence of four elements, covering Mo, Se, C and a small amount of O. The C 1s profile in Fig. 4b can be deconvoluted into two individual peaks at 284.8 (C-C) and 286.7 eV (C-OH) [39], respectively. As observed from Fig. 4c, the Mo 3d spectrum is fitted by two peaks at 229.2 and 232.3 eV, which correspond to the spin orbit peaks of Mo $3d_{5/2}$ and Mo $3d_{3/2}$ in $MoSe_2$/C composite, respectively, suggesting Mo IV state in the sample. Additionally, the Se 3d peak can be divided into two characteristic peaks at 54.7 and 55.6 eV, which belong to Se $3d_{5/2}$ and Se $3d_{3/2}$ peaks, respectively, revealing the −2 oxidation state for Se [26].

The electrode materials are assembled into coin cells to investigate their electrochemical performances as anode materials for LIBs and the result are shown in Fig. 5. The CV curves of $MoSe_2$/C composite in the initial three cycles are presented in Fig. 5a. In the first cycle, two reduction peaks at around 0.79 V and 0.36 V, and an oxidation peak at 2.2 V can be observed. The first reduction peak at 0.79 V which is shifted to 1.8 V in the following cycles is ascribed to the insertion of Li^+ into the $MoSe_2$ layers to form Li_xMoSe_2 [22,26]. The second reduction peak at 0.36 V is attributed to the phase conversion from Li_xMoSe_2 to Mo and Li_2Se and the formation of solid electrolyte interface (SEI) film [40,41]. The oxidation peak at 2.2 V is assigned to the oxidation from Mo to $MoSe_2$. The CV curves overlapped well in the following cycles, demonstrating the excellent stability and reversibility.

Fig. 5b displays the galvanostatic charge-discharge (GCD) profiles of selected cycles of the 1st, 2nd, 10th, 20th, and 40th cycles for LIBs at 200 mA g^{-1}. The discharge plateaus are around 0.79 and 0.36 V in the initial cycle and charge plateau located around 2.2 V, which are in good accordance with CV results. The cycling performances of the $MoSe_2$/C composite and $MoSe_2$ nanorods at 200 mA g^{-1} are demonstrated in Fig. 5c. The specific capacity of the $MoSe_2$ nanorods decreases from 536 mA h g^{-1} for the first cycle to 113 mA h g^{-1} after 100 cycles, possessing the inferior cycling stability. Interestingly, the specific capacity of the $MoSe_2$/C composite decreases slowly in the first 26 cycles, then increases steadily and retains 755 mA h g^{-1} after 200 cycles, which is higher than the

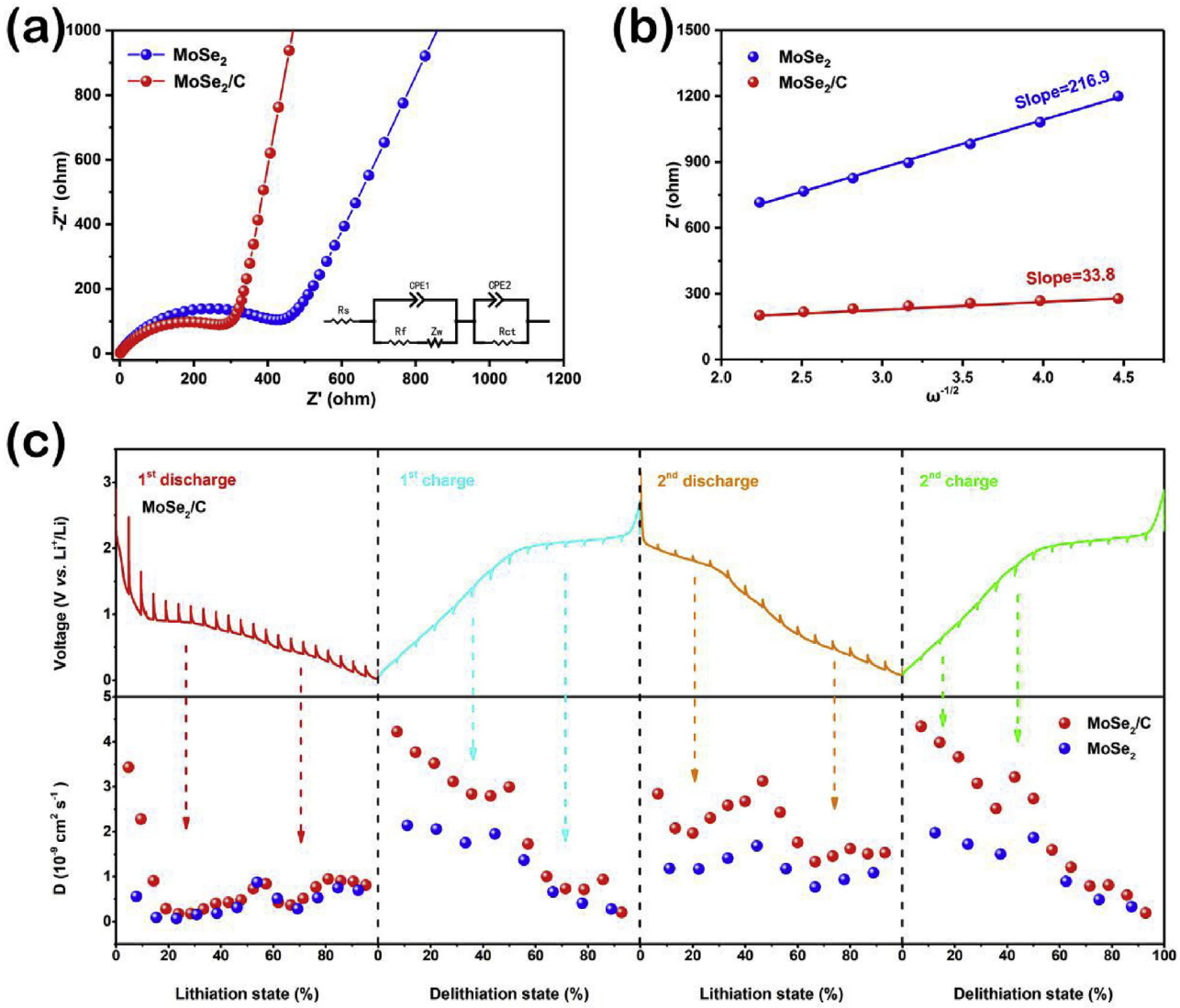

Fig. 6. (a) Nyquist plots of the as-synthesized $MoSe_2$/C composite and $MoSe_2$. The bottom inset is the corresponding equivalent circuit model; (b) the corresponding profile of the relationship between Z′ and $\omega^{-1/2}$ at low frequency region; (c) GITT curves and the corresponding Li^+ diffusion coefficient at different discharge/charge voltage of $MoSe_2$/C electrode.

initial reversible specific capacity (628 mA h g^{-1}). The initial falling may be caused by the formation of the SEI film and the followed rising might result from the activation of the active substance and the increment of the active sites [22,42]. The alternative current impedance measurements were conducted after 10, 20 and 50 cycles as shown in Fig. S4, and the R_{ct} value is 34.99 Ω, 46.42 Ω, and 33.9 Ω, respectively. The R_{ct} value after 20 cycles is higher than that after 10 cycles, which can be attributed to the decomposition of the electrolyte and the stabilization of SEI layer for the first 26 cycles. However, the R_{ct} value after 50 cycles is smaller, which may be attributed to the activation of the electrode materials after electrochemical grinding of the $MoSe_2$/C composite. To further verify the superior electrochemical performance of the $MoSe_2$/C composite, the rate performances of the $MoSe_2$/C and the $MoSe_2$ nanorods electrodes were performed and shown in Fig. 5d. The $MoSe_2$/C composite delivered the capacities of 451, 421, 396, 371, 326 and 208 mA h g^{-1} at 100, 200, 500, 1000, 2000, 5000 mA g^{-1}, respectively. After resetting the current density to 100 mA g^{-1}, a capacity of 557 mA h g^{-1} can be recovered. However, although the $MoSe_2$ nanorods electrode exhibit high capacity at low current densities, the capacities decrease quickly at high rates. In particular, only a capacity of 28 mA h g^{-1} can be delivered at the current density of 5000 mA g^{-1}. The results demonstrate the greatly improved rate capability of the $MoSe_2$/C nanorod composite.

The EIS and galvanostatic intermittent titration technique (GITT) measurements were conducted to better understand the intrinsic electrochemical and kinetic mechanisms of the $MoSe_2$/C composite. Fig. 6a displays the Nyquist plots of the $MoSe_2$/C composite and $MoSe_2$ nanorods. Both two samples' plots intuitively demonstrate a semicircle with an inclined line, which are simulated by the equivalent circuit model (inset in Fig. 6a) [23,43]. R_s stands for the electrolyte resistance, R_f and CPE1 represent the SEI layer resistance and the constant phase element, respectively. Z_w is the Warburg impedance, R_{ct} and CPE2 indicate the charge transfer resistance and related double layer capacitor, respectively. According to the fitting result, the R_{ct} value of $MoSe_2$/C composite is 332.8 Ω, which is smaller than that of $MoSe_2$ nanorods (458.1 Ω). On the basis of Eq. S(1) [44], the diffusion coefficient of Li^+ is in inverse proportion to σ, where σ is the slope of the line Z′-$\omega^{-1/2}$ (Eq. S(2)). As disclosed in Fig. 6b, contrary to the EIS pattern, the slope value of the $MoSe_2$/C composite (33.8) is smaller than that of $MoSe_2$ nanorods (216.9). The results demonstrate that the carbon-encapsulated $MoSe_2$

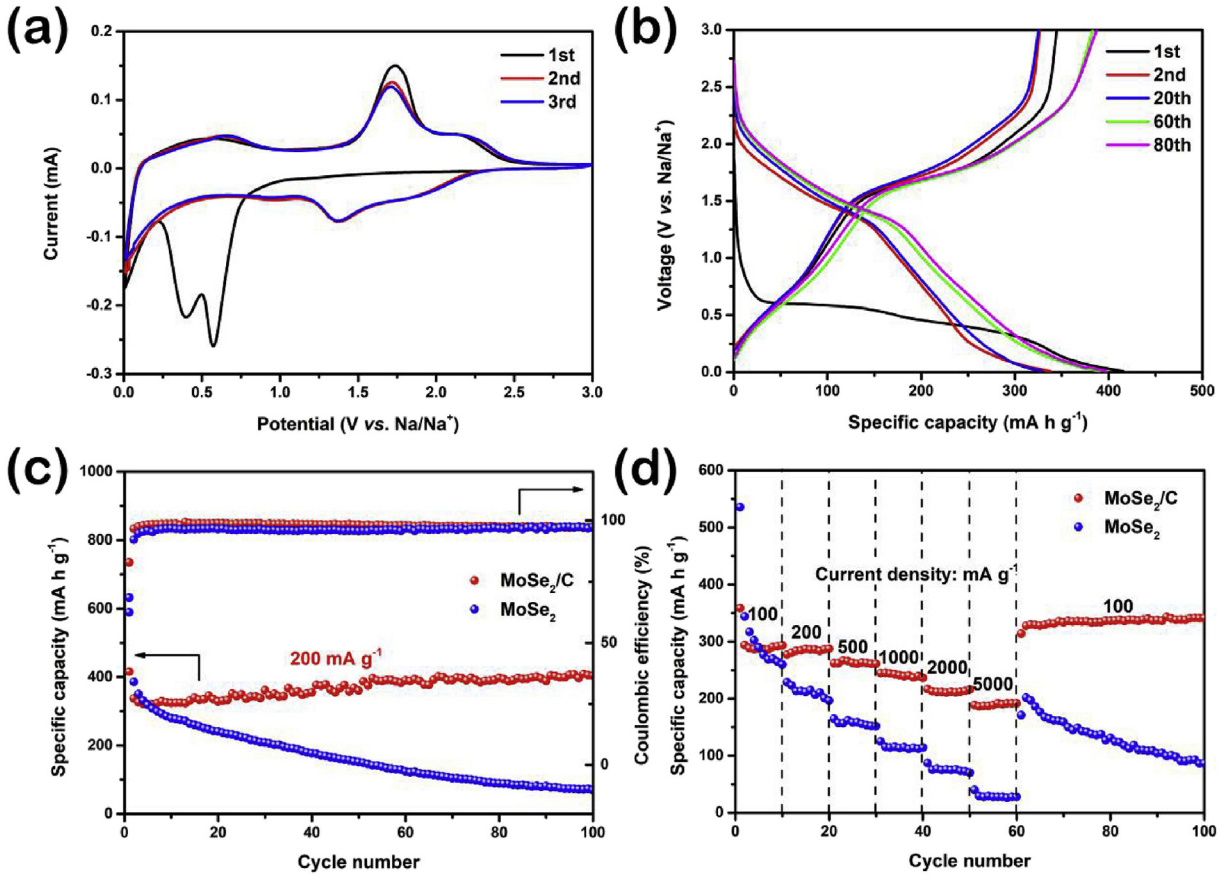

Fig. 7. Electrochemical performances for SIBs: (a) The initial three consecutive CV curves of $MoSe_2$/C at a scanning rate of 0.1 mV s^{-1} between 0.01 and 3 V vs Na/Na^+; (b) GCD profiles of the 1st, 2nd, 20th, 60th and 80th cycle at 200 mA g^{-1}; (c) cycling performances at 200 mA g^{-1}; (d) rate performances at the current densities of 100, 200, 500, 1000, 2000, 5000 mA g^{-1}.

nanorods with good crystallinity greatly facilitate the ion diffusion kinetics and electron transport rate. GITT tests were used to elucidate the effect of multistep de/lithiation on the ion diffusion and conductivity. The diffusion coefficients (D) at different discharge/charge voltages were calculated in the light of Fig. S5 and Eq. S(3) [45,46], and the results of the first two cycles are shown in Fig. 6c. The positions around 0.79 V and 0.36 V during the first discharge, and the position at around 2.2 V during the first charge (Fig. S6) are attributed to the Li^+ insertion and removal process. The $MoSe_2$/C composite has higher diffusion coefficient compared with $MoSe_2$ nanorods. The higher Li^+ diffusion coefficient of the $MoSe_2$/C is attributed to the carbon-encapsulated nanorod structure, which improved the electronic conductivity.

The SEM images of $MoSe_2$/C composite and $MoSe_2$ anodes after 100 cycles at 100 mA g^{-1} are shown in Fig. S7. The morphology of $MoSe_2$/C (Fig. S7a) are in good reservation, demonstrating the carbon-encapsulated nanorod structure could tolerate the volume variations upon cycling. However, the $MoSe_2$ nanorods morphology (Fig. S7b) aggregates or pulverizes seriously. The result demonstrates better structural stability of the $MoSe_2$/C composite electrode.

Moreover, the electrochemical properties of $MoSe_2$/C composite and $MoSe_2$ nanorods for SIBs were also explored and shown in Fig. 7. Fig. 7a presents the CV profiles of the $MoSe_2$/C composite in the first three cycles. Two cathodic peaks located at 0.57 V involved the intercalation reaction ($MoSe_2 + xNa^+ = Na_xMoSe_2$) [39] and 0.40 V involved the conversion reaction ($Na_xMoSe_2 + (4\text{-}x)Na^+ = Mo + 2Na_2Se$) and SEI film formation [19,39]. And one anodic peak appeared at 1.74 V involved the oxidation of Mo to $MoSe_2$. The GCD profiles exhibited in Fig. 7b are also in good agreement with the CV results. Fig. 7c exhibits the cycling performances of the $MoSe_2$/C composite and $MoSe_2$ nanorods for SIBs at 200 mA g^{-1}. The discharge capacity of $MoSe_2$/C composite delivers 416 mA h g^{-1} in the first cycle with a high coulombic efficiency of 82.9% and still keeps 404 mA h g^{-1} after 100 cycles. By contrast, the $MoSe_2$ nanorods displays an obvious declining trend during the cycling process, indicating the carbon coating can greatly improve the cycle stability. Fig. 7d depicts the rate performances of two anode materials at various current densities from 100 to 5000 mA g^{-1}, in which the capacity for $MoSe_2$/C composite gradually declined with the increase of the current density, and can recover to 342 mA h g^{-1} when returned to 100 mA g^{-1}. Nevertheless, the capacities for $MoSe_2$ nanorods sharply decreased and it was almost zero at 5000 mA g^{-1}. The $MoSe_2$/C composite nanorods exhibit much better capacity retention ability during the cycling process, which may be attributed to the improved structural stability of the electrode materials. Moreover, the better rate capability can be attributed to the electronic conductivity of the $MoSe_2$/C composite by the carbon coating layer.

4. Conclusion

In summary, $MoSe_2$/C nanorods composite were successfully prepared by using organic-inorganic hybrid MoO_x-EDA as a sacrificial template. The as-obtained $MoSe_2$/C composite exhibits excellent performances as anode materials for LIBs and SIBs. The good electrochemical performances are attributed to the smart $MoSe_2$/C nanorod composite with bicontinuous electron/ion

pathways, low charge transfer resistance, and robust structure stability.

Acknowledgements

This work was supported by National Natural Science Foundation of China (No. 51874162), Hunan Provincial Natural Science Foundation of China (2018JJ1036), the Innovation Project of Central South University (2017CX001), Central South University Postdoctoral Research Opening Fund.

Appendix A. Supplementary data

Supplementary data to this article can be found online at https://doi.org/10.1016/j.electacta.2018.09.154.

References

[1] B. Dunn, H. Kamath, J.M. Tarascon, Electrical energy storage for the grid: a battery of choices, Science 334 (2011) 928–935.
[2] Q. Wei, F. Xiong, S. Tan, L. Huang, E.H. Lan, B. Dunn, L. Mai, Porous one-dimensional nanomaterials: design, fabrication and applications in electrochemical energy storage, Adv. Mater. 29 (2017), 1602300.
[3] V. Etacheri, R. Marom, R. Elazari, G. Salitra, D. Aurbach, Challenges in the development of advanced Li-ion batteries: a review, Energy Environ. Sci. 4 (2011) 3243–3262.
[4] X. Cao, A. Pan, Y. Zhang, J. Li, Z. Luo, X. Yang, S. Liang, G. Cao, Nanorod-nanoflake interconnected $LiMnPO_4Li_3V_2(PO_4)_3$/C composite for high-rate and long-life lithium-ion batteries, ACS Appl. Mater. Interfaces 8 (2016) 27632–27641.
[5] S. Liang, X. Cao, Y. Wang, Y. Hu, A. Pan, G. Cao, Uniform $8LiFePO_4 \cdot Li_3V_2(PO_4)_3$/C nanoflakes for high-performance Li-ion batteries, Nano Energy 22 (2016) 48–58.
[6] K. Chang, W. Chen, L-cysteine-assisted synthesis of layered MoS_2/graphene composites with excellent electrochemical performances for lithium ion batteries, ACS Nano 5 (2011) 4720–4728.
[7] C. Zhao, J. Kong, X. Yao, X. Tang, Y. Dong, S.L. Phua, X. Lu, Thin MoS_2 nanoflakes encapsulated in carbon nanofibers as high-performance anodes for lithium-ion batteries, ACS Appl. Mater. Interfaces 6 (2014) 6392–6398.
[8] P. Zhang, L. Zou, H. Hu, M. Wang, J. Fang, Y. Lai, J. Li, 3D hierarchical carbon microflowers decorated with MoO_2 nanoparticles for lithium ion batteries, Electrochim. Acta 250 (2017) 219–227.
[9] J. Peters, D. Buchholz, S. Passerini, M. Weil, Life cycle assessment of sodium-ion batteries, Energy Environ. Sci. 9 (2016) 1744–1751.
[10] X. Cao, A. Pan, S. Liu, J. Zhou, S. Li, G. Cao, J. Liu, S. Liang, Chemical synthesis of 3D graphene-like cages for sodium-ion batteries applications, Adv. Energy Mater. 7 (2017) 1700797.
[11] J. Li, X. Cao, A. Pan, Y. Zhao, H. Yang, G. Cao, S. Liang, Nanoflake-assembled three-dimensional $Na_3V_2(PO_4)_3$/C cathode for high performance sodium ion batteries, Chem. Eng. J. 335 (2018) 301–308.
[12] Y. Cai, H. Yang, J. Zhou, Z. Luo, G. Fang, S. Liu, A. Pan, S. Liang, Nitrogen doped hollow MoS_2/C nanospheres as anode for long-life sodium-ion batteries, Chem. Eng. J. 327 (2017) 522–529.
[13] J. Goodenough, K. Park, The Li-ion rechargeable battery: a perspective, J. Am. Chem. Soc. 135 (2013) 1167–1176.
[14] H. Hou, C. Banks, M. Jing, Y. Zhang, X. Ji, Carbon quantum dots and their derivative 3D porous carbon frameworks for sodium-ion batteries with ultralong cycle life, Adv. Mater. 27 (2015) 7861–7866.
[15] G. Zou, H. Hou, G. Zhao, P. Ge, D. Yin, X. Ji, N-rich carbon coated $CoSnO_3$ derived from *in situ* construction of a Co–MOF with enhanced sodium storage performance, J. Mater. Chem. A 6 (2018) 4839–4847.
[16] M. Chhowalla, H. Shin, G. Eda, L. Li, K. Loh, H. Zhang, The chemistry of two-dimensional layered transition metal dichalcogenide nanosheets, Nat. Chem. 5 (2013) 263–275.
[17] P. Ge, H. Hou, C. Banks, C. Foster, S. Li, Y. Zhang, J. He, C. Zhang, X. Ji, Binding $MoSe_2$ with carbon constrained in carbonous nanosphere towards high-capacity and ultrafast Li/Na-ion storage, Energy Storage Mater. 12 (2018) 310–323.
[18] P. Zhang, F. Qin, L. Zou, M. Wang, K. Zhang, Y. Lai, J. Li, Few-layered MoS_2/C with expanding *d*-spacing as a high-performance anode for sodium-ion batteries, Nanoscale 9 (2017) 12189–12195.
[19] Y. Ko, S. Choi, S. Park, Y. Kang, Hierarchical $MoSe_2$ yolk-shell microspheres with superior Na-ion storage properties, Nanoscale 6 (2014) 10511–10515.
[20] J. Wang, L. Lu, M. Lotya, J. Coleman, S. Chou, H. Liu, A. Minett, J. Chen, Development of MoS_2-CNT composite thin film from layered MoS_2 for lithium batteries, Adv. Energy Mater. 3 (2013) 798–805.
[21] M. Zhu, Z. Luo, A. Pan, H. Yang, T. Zhu, S. Liang, G. Cao, N-doped one-dimensional carbonaceous backbones supported $MoSe_2$ nanosheets as superior electrodes for energy storage and conversion, Chem. Eng. J. 334 (2018) 2190–2200.
[22] Z. Luo, J. Zhou, L. Wang, G. Fang, A. Pan, S. Liang, Two-dimensional hybrid nanosheets of few layered $MoSe_2$ on reduced graphene oxide as anodes for long-cycle-life lithium-ion batteries, J. Mater. Chem. A 4 (2016) 15302–15308.
[23] H. Wang, X. Lan, D. Jiang, Y. Zhang, H. Zhong, Z. Zhang, Y. Jiang, Sodium storage and transport properties in pyrolysis synthesized $MoSe_2$ nanoplates for high performance sodium-ion batteries, J. Power Sources 283 (2015) 187–194.
[24] D. Xie, W. Tang, Y. Wang, X. Xia, Y. Zhong, D. Zhou, D. Wang, X. Wang, J. Tu, Facile fabrication of integrated three-dimensional C-$MoSe_2$/reduced graphene oxide composite with enhanced performance for sodium storage, Nano Res. 9 (2016) 1618–1629.
[25] J. Li, H. Hu, F. Qin, P. Zhang, L. Zou, H. Wang, K. Zhang, Y. Lai, Flower-like $MoSe_2$/C composite with expanded (0 0 2) planes of few-layer $MoSe_2$ as the anode for high-performance sodium-ion batteries, Chem. Eur. J. 23 (2017) 14004–14010.
[26] Y. Liu, M. Zhu, D. Chen, Sheet-like $MoSe_2$/C composites with enhanced Li-ion storage properties, J. Mater. Chem. A 3 (2015) 11857–11862.
[27] X. Yang, Z. Zhang, Y. Fu, Q. Li, Porous hollow carbon spheres decorated with molybdenum diselenide nanosheets as anodes for highly reversible lithium and sodium storage, Nanoscale 7 (2015) 10198–10203.
[28] B. Mao, T. Bao, J. Yu, L. Zheng, J. Qin, W. Yin, M. Cao, One-pot synthesis of $MoSe_2$ hetero-dimensional hybrid self-assembled by nanodots and nanosheets for electrocatalytic hydrogen evolution and photothermal therapy, Nano Res. 10 (2017) 2667–2682.
[29] X. Zhao, W. Cai, Y. Yang, X. Song, Z. Neale, H.-E. Wang, J. Sui, G. Cao, MoSe2 nanosheets perpendicularly grown on graphene with Mo–C bonding for sodium-ion capacitors, Nano Energy 47 (2018) 224–234.
[30] Y. Nien, J. Carey, J. Chen, Physical and electrochemical properties of $LiFePO_4$/C composite cathode prepared from various polymer-containing precursors, J. Power Sources 193 (2009) 822–827.
[31] Q. Gao, S. Wang, H. Fang, J. Weng, Y. Zhang, J. Mao, Y. Tang, One-dimensional growth of MoO_x-based organic–inorganic hybrid nanowires with tunable photochromic properties, J. Mater. Chem. 22 (2012) 4709–4715.
[32] S. Zhuo, Y. Xu, W. Zhao, J. Zhang, B. Zhang, Hierarchical nanosheet-based MoS_2 nanotubes fabricated by an anion-exchange reaction of MoO_3-amine hybrid nanowires, Angew. Chem. Int. Ed. 52 (2013) 8602–8606.
[33] K. Zhu, X. Wang, J. Liu, S. Lo, H. Wang, L. Yang, S. Liu, T. Xie, Novel amorphous MoS_2/MoO_3/Nitrogen-doped carbon composite with excellent electrochemical performance for lithium ion batteries and sodium ion batteries, ACS Sustain. Chem. Eng. 5 (2017) 8025–8034.
[34] Z. Che, Y. Li, K. Chen, M. Wei, Hierarchical MoS_2@RGO nanosheets for high performance sodium storage, J. Power Sources 331 (2016) 50–57.
[35] Y. Wu, M. Xu, X. Chen, S. Yang, H. Wu, J. Pan, X. Xiong, CTAB-assisted synthesis of novel ultrathin $MoSe_2$ nanosheets perpendicular to graphene for the adsorption and photodegradation of organic dyes under visible light, Nanoscale 8 (2016) 440–450.
[36] Y. Fang, L. Xiao, J. Qian, Y. Cao, X. Ai, Y. Huang, H. Yang, 3D Graphene Decorated $NaTi_2(PO_4)_3$ microspheres as a superior high-rate and ultracycle-stable anode material for sodium ion batteries, Adv. Energy Mater. 6 (2016), 1502197.
[37] Q. An, F. Xiong, Q. Wei, J. Sheng, L. He, D. Ma, Y. Yao, L. Mai, Nanoflake-assembled hierarchical $Na_3V_2(PO_4)_3$/C Microflowers: superior Li storage performance and insertion/extraction mechanism, Adv. Energy Mater. 5 (2015), 1401963.
[38] D. Choi, D. Wang, I. Bae, J. Xiao, Z. Nie, W. Wang, V. Viswanathan, Y. Lee, J. Zhang, G. Graff, Z. Yang, J. Liu, $LiMnPO_4$ nanoplate grown via solid-state reaction in molten hydrocarbon for Li-ion battery cathode, Nano Lett. 10 (2010) 2799–2805.
[39] Y. Tang, Z. Zhao, Y. Wang, Y. Dong, Y. Liu, X. Wang, J. Qiu, Carbon-stabilized interlayer-expanded few-layer $MoSe_2$ nanosheets for sodium ion batteries with enhanced rate capability and cycling performance, ACS Appl. Mater. Interfaces 8 (2016) 32324–32332.
[40] L. Ma, X.P. Zhou, L.M. Xu, X.Y. Xu, L.L. Zhang, W.X. Chen, Ultrathin few-layered molybdenum selenide/graphene hybrid with superior electrochemical Li-storage performance, J. Power Sources 285 (2015) 274–280.
[41] L. Yang, S. Wang, J. Mao, J. Deng, Q. Gao, Y. Tang, O.G. Schmidt, Hierarchical MoS_2/polyaniline nanowires with excellent electrochemical performance for lithium-ion batteries, Adv. Mater. 25 (2013) 1180–1184.
[42] K. Chang, D. Geng, X. Li, J. Yang, Y. Tang, M. Cai, R. Li, X. Sun, Ultrathin MoS_2/nitrogen-doped graphene nanosheets with highly reversible lithium storage, Adv. Energy Mater. 3 (2013) 839–844.
[43] Y. Wang, G. Xing, Z. Han, Y. Shi, J. Wong, Z. Huang, K. Ostrikov, H. Yang, Pre-lithiation of onion-like carbon/MoS_2 nano-urchin anodes for high-performance rechargeable lithium ion batteries, Nanoscale 6 (2014) 8884–8890.
[44] X. Kong, Y. Wang, J. Lin, S. Liang, A. Pan, G. Cao, Twin-nanoplate assembled hierarchical Ni/MnO porous microspheres as advanced anode materials for lithium-ion batteries, Electrochim. Acta 259 (2018) 419–426.
[45] B. Yin, X. Cao, A. Pan, Z. Luo, S. Dinesh, J. Lin, Y. Tang, S. Liang, G. Cao, Encapsulation of CoS_x nanocrystals into N/S Co-doped honeycomb-like 3D porous carbon for high-performance lithium storage, Adv. Sci. (2018), 1800829.
[46] G. Fang, Z. Wu, J. Zhou, C. Zhu, X. Cao, T. Lin, Y. Chen, C. Wang, A. Pan, S. Liang, Observation of pseudocapacitive effect and fast ion diffusion in bimetallic sulfides as an advanced sodium-ion battery anode, Adv. Energy Mater. 8 (2018), 1703155.